OPTIMIZING DUTY RATIOS IN A GRID-INTERACTIVE INVERTER: A FIVE-LEVEL, THREE-LEG, THREE-PHASE CASCADED H-BRIDGE APPROACH EMPLOYING MPCC WITH AN EXPLICIT INTEGRATION ALGORITHM

Edmund Kwafo **ADJEI-SAFORO**[1], Francis Boafo **EFFAH**[1], Misbawu **ADAM**[2], Ebrahimpanah **SHAHROUZ**[3], Emmanuel Asuming **FRIMPONG**[1]

[1] *Kwame Nkrumah Unversity of Science and Technology,* [2] *Kumasi Technical University,* [3]*Wuhan University of Technology*

ekadjeisaforo@st.knust.edu.gh, kingacid17@gmail.com, adam.misbawu@kstu.edu.gh

Keywords: Total harmonic distortion, three level three-leg, model predictive current control

Abstract*: The model predictive current control stands out as a robust control strategy extensively applied in the enhancement of various industrial applications. Renowned for its capacity to handle multiple inputs and generate multiple outputs (MIMO), it is recognized for its consistently excellent performance and unique stable control techniques. However, the computational intensity required to remedy an optimization task at each time step poses a potential drawback, impacting its suitability for real-time control applications and potentially affecting system performance. This study introduces the concept of duty cycle optimization, leveraging the explicit integration approximation. This involves the application of rectangular voltage for both non-zero as well as zero within one control period to minimize current ripples in the grid-interactive system. Additionally, error minimization is achieved through the selection of the duration for the two-rectangular voltage. Experimental and simulation results validate the substantial reductions in ripple current as well as total harmonic distortion achieved through this approach.*

1. INTRODUCTION

To meet the growing electricity demands of end-users and enhance the current power generation capacity, an increasing amount of renewable energy, notably solar and wind power to a greater extent, is being integrated into the grids [1, 2].

Recently, the integration of renewable energy systems into the grid has been achieved by employing multilevel inverters. This choice is attributed to their benefits, including low electromagnetic compatibility and switching losses, as well as high voltage handling capabilities and waveform quality [3, 4, 24]. Multilevel inverters fall into three main categories: flying capacitor, diode-clamped, and cascaded H-bridge (CHB) [5-7]. Model Predictive Control (MPC) comes in two variations: Finite Control Set and Continuous Control Set. The former, recognized as a modern control technique, stands out for its capability to address variable constraints and nonlinearities within a system. Notably, it demonstrates swift control responses to dynamic systems and predicts the future characteristics of a system by minimizing a cost function [9, 10, 18]. Model Predictive Current Control (MPCC), falling under the umbrella of MPC, holds a distinguished status as one of the leading control methods for power converters [22, 23].

This paper focuses on designing Model Predictive Current Control (MPCC) with duty cycle optimization using the Explicit Integration Algorithm for a five-level three-leg three-phase (FTT) cascaded H-Bridge (CHB) interactive inverter with LCL smoother output. To achieve a rapid dynamic response and enhanced steady-state performance, the utilization of both zero and non-zero rectangular voltages within a single control period is recommended. The duration of the non-zero rectangular voltage is determined based on the reduction of current error at the end of the subsequent control duration [14, 17, 18, 20]. The subsequent chapters of the paper are organized as follows: Chapter 2 delves into the five-level three-leg three-phase cascaded H-Bridge inverter with LCL smoother output. Chapter 3 introduces MPCC with duty cycle optimization based on explicit integration approximation. Simulation and experimental results are presented in Chapters 4 and 5 respectively. Finally, Chapter 6 concludes the paper.

2. FIVE-LEVEL THREE-LEG THREE-PHASE (FTT) CHB INVERTER FEATURING LCL SMOOTHER OUTPUT

Figure 1 illustrates a schematic diagram of a FTTCHB grid-interactive inverter with an LCL smoother output. Within the five-level cascaded inverter, each cell is distinct, having its own dedicated DC source and H-bridge inverter [7]. Each cell contributes $V_{dc}/_2$ to the total input DC voltage, denoted as V_{dc}. Then each full-bridge inverter can switch between $V_{dc}/_2$, 0, $-V_{dc}/_2$.

The formula for voltage levels in relation to the number of output phases is provided as follows:

$$m = (2n + 1) \tag{1}$$

where DC source is characterised by n numbers of secluded DC sources. In a FTTCHB inverter, for one cell, the four switches S_1, S_2, S_1' and S_2' are controlled to generate three discreet outputs V_{out} with levels $V_{dc}/_2$, 0, $-V_{dc}/_2$. When When $S_1$and $\boldsymbol{S_2'}$are on, the output is $V_{dc}/_2$; when S_2 and $\boldsymbol{S_1'}$are on, the output is $-V_{dc}/_2$; when either pair S_1 and S_2 or $\boldsymbol{S_1'}$and $\boldsymbol{S_2'}$ are on, the output is 0 [8]. Therefore for having 2 separated DC sources, five possible voltage levels, V_{dc}, $V_{dc}/_2$, 0, $-V_{dc}/_2$, $-V_{dc}$ are created.

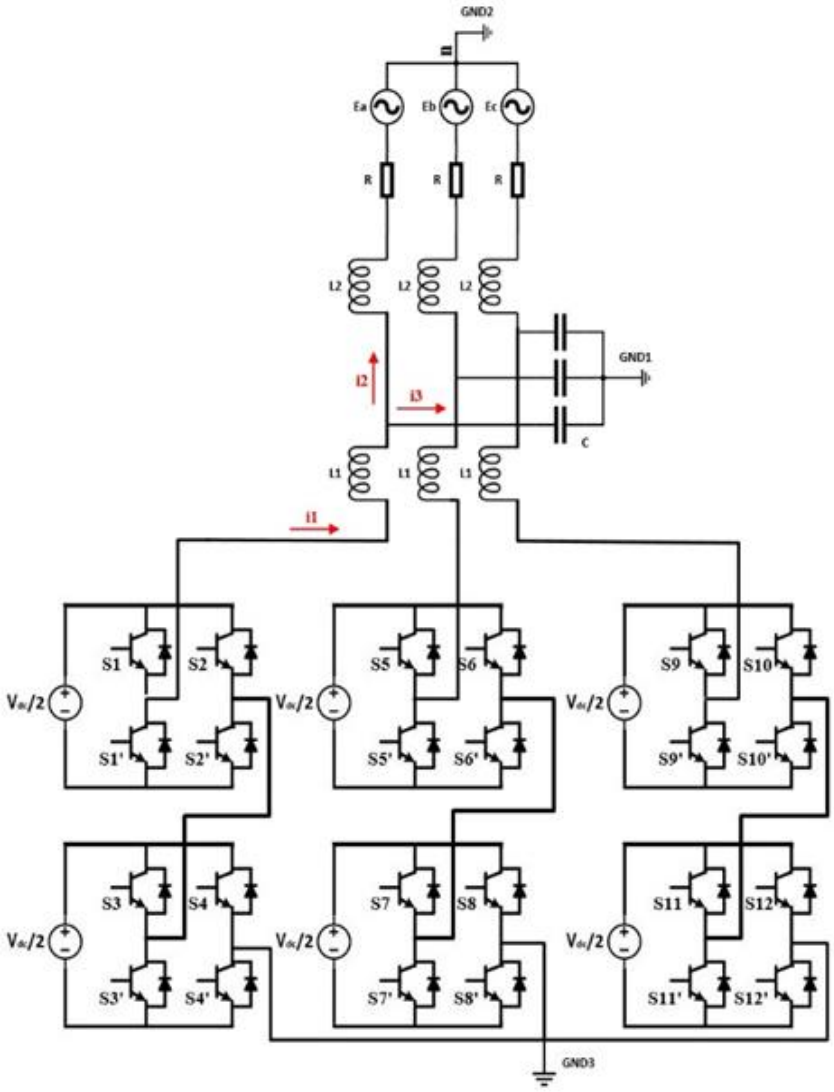

Figure 1. FTT CHB inverter

The output rectangular voltage can be written as:

$$V = \frac{2}{3}(V_{aN} + \alpha V_{bN} + \alpha^2 V_{cN}) \tag{2}$$

where $= e^{j\frac{2\pi}{3}}, \alpha = -\frac{1}{2} + j\frac{\sqrt{3}}{2}$, which represent 120° phase displacement between the phases: V_{aN}, V_{bN} and V_{cN}. The subscripts used denote the phase quantities of the inverter, and the

negative terminal of the DC link is represented by N [9], [24]. By replacing a in equation (2) output voltage vector is calculated as follow:

$$V = \frac{2}{3}V_{aN} - \frac{1}{3}V_{bN} + \mathrm{j}\frac{\sqrt{3}}{3}V_{bN} - \frac{1}{3}V_{cN} - \mathrm{j}\frac{\sqrt{3}}{3}V_{cN} \tag{3}$$

The calculation of the number of voltage level combinations k_m is based on $k_m = 3^m$. Therefore, considering all potential combinations of gating signals for two cells in the three-phase CHB inverter, 125 switching states and corresponding 125 rectangular voltages are obtained (refer to Table 1). However, 64 of these rectangular voltages are redundant, leaving only 61 non-redundant rectangular voltages, as calculated below.

$$k_V = 12C^2 + 6C + 1 \tag{4}$$

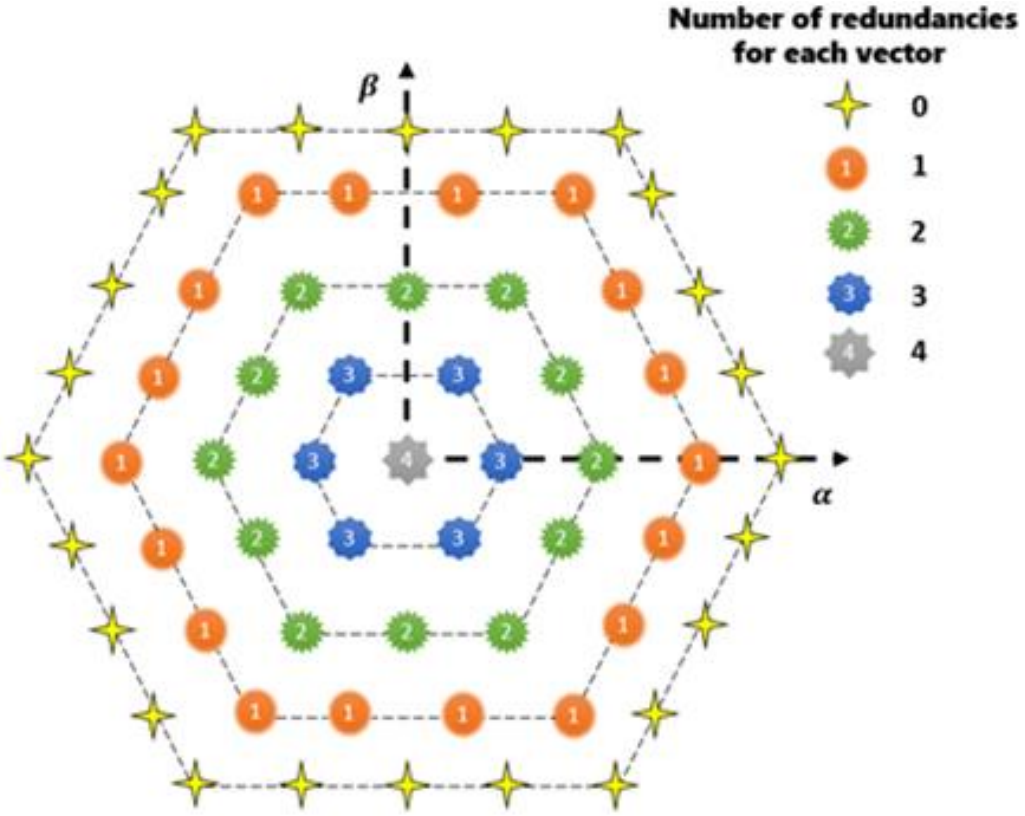

Figure 2. Rectangular voltages for FTT CHB inverter

C represents the number of cells in each leg of the CHB inverter, and k_V denotes the quantity of non-redundant voltage vectors (refer to *figure 2*).

As the impedance of C is considerably larger than the impedance of L_1 and L_2, the current flowing through C can be neglected. Thus, it can be expressed as [11]:

$$i_3 = 0,\ i_1 = i_2 = i \tag{5}$$

The dynamics of the grid-side current for each phase can be expressed as follows:

$$\begin{cases} V_{an} = L\frac{di_a}{dt} + Ri_a + e_a \\ V_{bn} = L\frac{di_b}{dt} + Ri_b + e_b \\ V_{cn} = L\frac{di_c}{dt} + Ri_c + e_c \end{cases} \quad (6)$$

where R represents the filter resistance and $L = L_1 + L_2$. By substituting (6) into (2), a vector equation expressing the relationship between various parameters for the grid side can be formulated:

$$V = L\frac{d(^2/_3(i_a+ai_b+a^2i_c))}{dt} + R(^2/_3(i_a + ai_b + a^2i_c)) + {}^2/_3(e_a + ae_b + a^2e_c) \quad (7)$$

where: $a = e^{j\frac{2\pi}{3}}$, $a = -\frac{1}{2} + j\frac{\sqrt{3}}{2}$, $i = {}^2/_3(i_a + ai_b + a^2i_c)$ and $e = {}^2/_3(e_a + ae_b + a^2e_c$. Therefore, the system depicted in *figure 1* can be represented by the differential rectangular equation:

$$V = L\frac{di}{dt} + Ri + e \quad (8)$$

In this context, V denotes the rectangular voltage produced by the inverter, i represents rectangular current on the grid-side, and e denotes the rectangular voltage on the grid-side [10].

Table 1. Rectangular voltages and their switching states

V_{aN}	V_{bN}	V_{cN}	Voltage vector	V_{aN}	V_{bN}	V_{cN}	Voltage vector	V_{aN}	V_{bN}	V_{cN}	Voltage vector
0	0	0	0	V_{dc}	$-V_{dc}$	0	$V_{dc} - j\frac{\sqrt{3}}{3}V_{dc}$	$-V_{dc}$	V_{dc}	0	$-V_{dc} + j\frac{\sqrt{3}}{3}V_{dc}$
0	0	V_{dc}	$-\frac{1}{3}V_{dc} - j\frac{\sqrt{3}}{3}V_{dc}$	V_{dc}	$-V_{dc}$	V_{dc}	$\frac{2}{3}V_{dc} - j\frac{2\sqrt{3}}{3}V_{dc}$	$-V_{dc}$	V_{dc}	V_{dc}	$-\frac{4}{3}V_{dc}$
0	0	$\frac{V_{dc}}{2}$	$-\frac{1}{6}V_{dc} - j\frac{\sqrt{3}}{6}V_{dc}$	V_{dc}	$-V_{dc}$	$\frac{V_{dc}}{2}$	$\frac{5}{6}V_{dc} - j\frac{\sqrt{3}}{2}V_{dc}$	$-V_{dc}$	V_{dc}	$\frac{V_{dc}}{2}$	$-\frac{7}{6}V_{dc} + j\frac{\sqrt{3}}{6}V_{dc}$
0	0	$-V_{dc}$	$\frac{1}{3}V_{dc} + j\frac{\sqrt{3}}{3}V_{dc}$	V_{dc}	$-V_{dc}$	$-V_{dc}$	$\frac{4}{3}V_{dc}$	$-V_{dc}$	V_{dc}	$-V_{dc}$	$-\frac{2}{3}V_{dc} + j\frac{2\sqrt{3}}{3}V_{dc}$
0	0	$-\frac{V_{dc}}{2}$	$\frac{1}{6}V_{dc} + j\frac{\sqrt{3}}{6}V_{dc}$	V_{dc}	$-V_{dc}$	$-\frac{V_{dc}}{2}$	$\frac{7}{6}V_{dc} - j\frac{\sqrt{3}}{6}V_{dc}$	$-V_{dc}$	V_{dc}	$-\frac{V_{dc}}{2}$	$-\frac{5}{6}V_{dc} + j\frac{\sqrt{3}}{2}V_{dc}$
0	V_{dc}	0	$-\frac{1}{3}V_{dc} + j\frac{\sqrt{3}}{3}V_{dc}$	V_{dc}	$-\frac{V_{dc}}{2}$	0	$\frac{5}{6}V_{dc} - j\frac{\sqrt{3}}{6}V_{dc}$	$-V_{dc}$	$\frac{V_{dc}}{2}$	0	$-\frac{5}{6}V_{dc} + j\frac{\sqrt{3}}{6}V_{dc}$
0	V_{dc}	V_{dc}	$-\frac{2}{3}V_{dc}$	V_{dc}	$-\frac{V_{dc}}{2}$	V_{dc}	$\frac{1}{2}V_{dc} - j\frac{\sqrt{3}}{2}V_{dc}$	$-V_{dc}$	$\frac{V_{dc}}{2}$	V_{dc}	$-\frac{7}{6}V_{dc} - j\frac{\sqrt{3}}{6}V_{dc}$
0	V_{dc}	$\frac{V_{dc}}{2}$	$-\frac{1}{2}V_{dc} + j\frac{\sqrt{3}}{6}V_{dc}$	V_{dc}	$-\frac{V_{dc}}{2}$	$\frac{V_{dc}}{2}$	$\frac{2}{3}V_{dc} - j\frac{\sqrt{3}}{3}V_{dc}$	$-V_{dc}$	$\frac{V_{dc}}{2}$	$\frac{V_{dc}}{2}$	$-V_{dc}$
0	V_{dc}	$-V_{dc}$	$j\frac{2\sqrt{3}}{3}V_{dc}$	V_{dc}	$-\frac{V_{dc}}{2}$	$-V_{dc}$	$\frac{7}{6}V_{dc} + j\frac{\sqrt{3}}{6}V_{dc}$	$-V_{dc}$	$\frac{V_{dc}}{2}$	$-V_{dc}$	$-\frac{1}{2}V_{dc} + j\frac{\sqrt{3}}{2}V_{dc}$
0	V_{dc}	$-\frac{V_{dc}}{2}$	$-\frac{1}{6}V_{dc} + j\frac{\sqrt{3}}{2}V_{dc}$	V_{dc}	$-\frac{V_{dc}}{2}$	$-\frac{V_{dc}}{2}$	V_{dc}	$-V_{dc}$	$\frac{V_{dc}}{2}$	$-\frac{V_{dc}}{2}$	$-\frac{2}{3}V_{dc} + j\frac{\sqrt{3}}{3}V_{dc}$
0	$\frac{V_{dc}}{2}$	0	$-\frac{1}{6}V_{dc} + j\frac{\sqrt{3}}{6}V_{dc}$	$\frac{V_{dc}}{2}$	0	0	$\frac{1}{3}V_{dc}$	$-V_{dc}$	$-V_{dc}$	0	$-\frac{1}{3}V_{dc} - j\frac{\sqrt{3}}{3}V_{dc}$
0	$\frac{V_{dc}}{2}$	V_{dc}	$-\frac{1}{2}V_{dc} - j\frac{\sqrt{3}}{6}V_{dc}$	$\frac{V_{dc}}{2}$	0	V_{dc}	$-j\frac{\sqrt{3}}{3}V_{dc}$	$-V_{dc}$	$-V_{dc}$	V_{dc}	$-\frac{2}{3}V_{dc} - j\frac{2\sqrt{3}}{3}V_{dc}$
0	$\frac{V_{dc}}{2}$	$\frac{V_{dc}}{2}$	$-\frac{1}{3}V_{dc}$	$\frac{V_{dc}}{2}$	0	$\frac{V_{dc}}{2}$	$\frac{1}{6}V_{dc} - j\frac{\sqrt{3}}{6}V_{dc}$	$-V_{dc}$	$-V_{dc}$	$\frac{V_{dc}}{2}$	$-\frac{1}{2}V_{dc} - j\frac{\sqrt{3}}{2}V_{dc}$

V_{aN}	V_{bN}	V_{cN}	Voltage vector	V_{aN}	V_{bN}	V_{cN}	Voltage vector	V_{aN}	V_{bN}	V_{cN}	Voltage vector
0	$\frac{V_{dc}}{2}$	$-V_{dc}$	$\frac{1}{6}V_{dc}+j\frac{\sqrt{3}}{2}V_{dc}$	$\frac{V_{dc}}{2}$	0	$-V_{dc}$	$\frac{2}{3}V_{dc}+j\frac{\sqrt{3}}{3}V_{dc}$	$-V_{dc}$	$-V_{dc}$	$-V_{dc}$	0
0	$\frac{V_{dc}}{2}$	$-\frac{V_{dc}}{2}$	$j\frac{\sqrt{3}}{3}V_{dc}$	$\frac{V_{dc}}{2}$	0	$-\frac{V_{dc}}{2}$	$\frac{1}{2}V_{dc}+j\frac{\sqrt{3}}{6}V_{dc}$	$-V_{dc}$	$-V_{dc}$	$-\frac{V_{dc}}{2}$	$-\frac{1}{6}V_{dc}-j\frac{\sqrt{3}}{6}V_{dc}$
0	$-V_{dc}$	0	$\frac{1}{3}V_{dc}-j\frac{\sqrt{3}}{3}V_{dc}$	$\frac{V_{dc}}{2}$	V_{dc}	0	$j\frac{\sqrt{3}}{3}V_{dc}$	$-V_{dc}$	$-\frac{V_{dc}}{2}$	0	$-\frac{1}{2}V_{dc}-j\frac{\sqrt{3}}{6}V_{dc}$
0	$-V_{dc}$	V_{dc}	$-j\frac{2\sqrt{3}}{3}V_{dc}$	$\frac{V_{dc}}{2}$	V_{dc}	V_{dc}	$-\frac{1}{3}V_{dc}$	$-V_{dc}$	$-\frac{V_{dc}}{2}$	V_{dc}	$-\frac{5}{6}V_{dc}-j\frac{\sqrt{3}}{2}V_{dc}$
0	$-V_{dc}$	$\frac{V_{dc}}{2}$	$\frac{1}{6}V_{dc}-j\frac{\sqrt{3}}{2}V_{dc}$	$\frac{V_{dc}}{2}$	V_{dc}	$\frac{V_{dc}}{2}$	$-\frac{1}{6}V_{dc}+j\frac{\sqrt{3}}{6}V_{dc}$	$-V_{dc}$	$-\frac{V_{dc}}{2}$	$\frac{V_{dc}}{2}$	$-\frac{2}{3}V_{dc}-j\frac{\sqrt{3}}{3}V_{dc}$
0	$-V_{dc}$	$-V_{dc}$	$\frac{2}{3}V_{dc}$	$\frac{V_{dc}}{2}$	V_{dc}	$-V_{dc}$	$\frac{1}{3}V_{dc}+j\frac{2\sqrt{3}}{3}V_{dc}$	$-V_{dc}$	$-\frac{V_{dc}}{2}$	$-V_{dc}$	$-\frac{1}{6}V_{dc}+j\frac{\sqrt{3}}{6}V_{dc}$
0	$-V_{dc}$	$-\frac{V_{dc}}{2}$	$\frac{1}{2}V_{dc}-j\frac{\sqrt{3}}{6}V_{dc}$	$\frac{V_{dc}}{2}$	V_{dc}	$-\frac{V_{dc}}{2}$	$\frac{1}{6}V_{dc}+j\frac{\sqrt{3}}{2}V_{dc}$	$-V_{dc}$	$-\frac{V_{dc}}{2}$	$-\frac{V_{dc}}{2}$	$-\frac{1}{3}V_{dc}$
0	$-\frac{V_{dc}}{2}$	0	$\frac{1}{6}V_{dc}-j\frac{\sqrt{3}}{6}V_{dc}$	$\frac{V_{dc}}{2}$	$\frac{V_{dc}}{2}$	0	$\frac{1}{6}V_{dc}+j\frac{\sqrt{3}}{6}V_{dc}$	$-\frac{V_{dc}}{2}$	0	0	$-\frac{1}{3}V_{dc}$
0	$-\frac{V_{dc}}{2}$	V_{dc}	$-\frac{1}{6}V_{dc}-j\frac{\sqrt{3}}{2}V_{dc}$	$\frac{V_{dc}}{2}$	$\frac{V_{dc}}{2}$	V_{dc}	$-\frac{1}{6}V_{dc}-j\frac{\sqrt{3}}{6}V_{dc}$	$-\frac{V_{dc}}{2}$	0	V_{dc}	$-\frac{2}{3}V_{dc}-j\frac{\sqrt{3}}{3}V_{dc}$
0	$-\frac{V_{dc}}{2}$	$\frac{V_{dc}}{2}$	$-j\frac{\sqrt{3}}{3}V_{dc}$	$\frac{V_{dc}}{2}$	$\frac{V_{dc}}{2}$	$\frac{V_{dc}}{2}$	0	$-\frac{V_{dc}}{2}$	0	$\frac{V_{dc}}{2}$	$-\frac{1}{2}V_{dc}-j\frac{\sqrt{3}}{6}V_{dc}$
0	$-\frac{V_{dc}}{2}$	$-V_{dc}$	$\frac{1}{2}V_{dc}+j\frac{\sqrt{3}}{6}V_{dc}$	$\frac{V_{dc}}{2}$	$\frac{V_{dc}}{2}$	$-V_{dc}$	$\frac{1}{2}V_{dc}+j\frac{\sqrt{3}}{2}V_{dc}$	$-\frac{V_{dc}}{2}$	0	$-V_{dc}$	$j\frac{\sqrt{3}}{3}V_{dc}$
0	$-\frac{V_{dc}}{2}$	$-\frac{V_{dc}}{2}$	$\frac{1}{3}V_{dc}$	$\frac{V_{dc}}{2}$	$\frac{V_{dc}}{2}$	$-\frac{V_{dc}}{2}$	$\frac{1}{3}V_{dc}+j\frac{\sqrt{3}}{3}V_{dc}$	$-\frac{V_{dc}}{2}$	0	$-\frac{V_{dc}}{2}$	$-\frac{1}{6}V_{dc}+j\frac{\sqrt{3}}{6}V_{dc}$
V_{dc}	0	0	$\frac{2}{3}V_{dc}$	$\frac{V_{dc}}{2}$	$-V_{dc}$	0	$\frac{2}{3}V_{dc}-j\frac{\sqrt{3}}{3}V_{dc}$	$-\frac{V_{dc}}{2}$	V_{dc}	0	$-\frac{2}{3}V_{dc}+j\frac{\sqrt{3}}{3}V_{dc}$
V_{dc}	0	V_{dc}	$\frac{1}{3}V_{dc}-j\frac{\sqrt{3}}{3}V_{dc}$	$\frac{V_{dc}}{2}$	$-V_{dc}$	V_{dc}	$\frac{1}{3}V_{dc}-j\frac{2\sqrt{3}}{3}V_{dc}$	$-\frac{V_{dc}}{2}$	V_{dc}	V_{dc}	$-V_{dc}$
V_{dc}	0	$\frac{V_{dc}}{2}$	$\frac{1}{2}V_{dc}-j\frac{\sqrt{3}}{6}V_{dc}$	$\frac{V_{dc}}{2}$	$-V_{dc}$	$\frac{V_{dc}}{2}$	$\frac{1}{2}V_{dc}-j\frac{\sqrt{3}}{2}V_{dc}$	$-\frac{V_{dc}}{2}$	V_{dc}	$\frac{V_{dc}}{2}$	$-\frac{5}{6}V_{dc}+j\frac{\sqrt{3}}{6}V_{dc}$
V_{dc}	0	$-V_{dc}$	$V_{dc}+j\frac{\sqrt{3}}{3}V_{dc}$	$\frac{V_{dc}}{2}$	$-V_{dc}$	$-V_{dc}$	V_{dc}	$-\frac{V_{dc}}{2}$	V_{dc}	$-V_{dc}$	$-\frac{1}{3}V_{dc}+j\frac{2\sqrt{3}}{3}V_{dc}$
V_{dc}	0	$-\frac{V_{dc}}{2}$	$\frac{5}{6}V_{dc}+j\frac{\sqrt{3}}{6}V_{dc}$	$\frac{V_{dc}}{2}$	$-V_{dc}$	$-\frac{V_{dc}}{2}$	$\frac{5}{6}V_{dc}-j\frac{\sqrt{3}}{6}V_{dc}$	$-\frac{V_{dc}}{2}$	V_{dc}	$-\frac{V_{dc}}{2}$	$-\frac{1}{2}V_{dc}+j\frac{\sqrt{3}}{2}V_{dc}$
V_{dc}	V_{dc}	0	$\frac{1}{3}V_{dc}+j\frac{\sqrt{3}}{3}V_{dc}$	$\frac{V_{dc}}{2}$	$-\frac{V_{dc}}{2}$	0	$\frac{1}{2}V_{dc}-j\frac{\sqrt{3}}{6}V_{dc}$	$-\frac{V_{dc}}{2}$	$\frac{V_{dc}}{2}$	0	$-\frac{1}{2}V_{dc}+j\frac{\sqrt{3}}{6}V_{dc}$
V_{dc}	V_{dc}	V_{dc}	0	$\frac{V_{dc}}{2}$	$-\frac{V_{dc}}{2}$	V_{dc}	$\frac{1}{6}V_{dc}-j\frac{\sqrt{3}}{2}V_{dc}$	$-\frac{V_{dc}}{2}$	$\frac{V_{dc}}{2}$	V_{dc}	$-\frac{5}{6}V_{dc}-j\frac{\sqrt{3}}{6}V_{dc}$
V_{dc}	V_{dc}	$\frac{V_{dc}}{2}$	$\frac{1}{6}V_{dc}+j\frac{\sqrt{3}}{6}V_{dc}$	$\frac{V_{dc}}{2}$	$-\frac{V_{dc}}{2}$	$\frac{V_{dc}}{2}$	$\frac{1}{3}V_{dc}-j\frac{\sqrt{3}}{3}V_{dc}$	$-\frac{V_{dc}}{2}$	$\frac{V_{dc}}{2}$	$\frac{V_{dc}}{2}$	$-\frac{2}{3}V_{dc}$
V_{dc}	V_{dc}	$-V_{dc}$	$\frac{2}{3}V_{dc}+j\frac{2\sqrt{3}}{3}V_{dc}$	$\frac{V_{dc}}{2}$	$-\frac{V_{dc}}{2}$	$-V_{dc}$	$\frac{5}{6}V_{dc}+j\frac{\sqrt{3}}{6}V_{dc}$	$-\frac{V_{dc}}{2}$	$\frac{V_{dc}}{2}$	$-V_{dc}$	$-\frac{1}{6}V_{dc}+j\frac{\sqrt{3}}{2}V_{dc}$
V_{dc}	V_{dc}	$-\frac{V_{dc}}{2}$	$\frac{1}{2}V_{dc}+j\frac{\sqrt{3}}{2}V_{dc}$	$\frac{V_{dc}}{2}$	$-\frac{V_{dc}}{2}$	$-\frac{V_{dc}}{2}$	$\frac{2}{3}V_{dc}$	$-\frac{V_{dc}}{2}$	$\frac{V_{dc}}{2}$	$-\frac{V_{dc}}{2}$	$-\frac{1}{3}V_{dc}+j\frac{\sqrt{3}}{3}V_{dc}$
V_{dc}	$\frac{V_{dc}}{2}$	0	$\frac{1}{2}V_{dc}+j\frac{\sqrt{3}}{6}V_{dc}$	$-V_{dc}$	0	0	$-\frac{2}{3}V_{dc}$	$-\frac{V_{dc}}{2}$	$-V_{dc}$	0	$-j\frac{\sqrt{3}}{3}V_{dc}$
V_{dc}	$\frac{V_{dc}}{2}$	V_{dc}	$\frac{1}{6}V_{dc}-j\frac{\sqrt{3}}{6}V_{dc}$	$-V_{dc}$	0	V_{dc}	$-V_{dc}-j\frac{\sqrt{3}}{3}V_{dc}$	$-\frac{V_{dc}}{2}$	$-V_{dc}$	V_{dc}	$-\frac{1}{3}V_{dc}-j\frac{2\sqrt{3}}{3}V_{dc}$
V_{dc}	$\frac{V_{dc}}{2}$	$\frac{V_{dc}}{2}$	$\frac{1}{3}V_{dc}$	$-V_{dc}$	0	$\frac{V_{dc}}{2}$	$-\frac{5}{6}V_{dc}-j\frac{\sqrt{3}}{6}V_{dc}$	$-\frac{V_{dc}}{2}$	$-V_{dc}$	$\frac{V_{dc}}{2}$	$-\frac{1}{6}V_{dc}-j\frac{\sqrt{3}}{2}V_{dc}$
V_{dc}	$\frac{V_{dc}}{2}$	$-V_{dc}$	$\frac{5}{6}V_{dc}+j\frac{\sqrt{3}}{2}V_{dc}$	$-V_{dc}$	0	$-V_{dc}$	$-\frac{1}{3}V_{dc}+j\frac{\sqrt{3}}{3}V_{dc}$	$-\frac{V_{dc}}{2}$	$-V_{dc}$	$-V_{dc}$	$\frac{1}{3}V_{dc}$
V_{dc}	$\frac{V_{dc}}{2}$	$-\frac{V_{dc}}{2}$	$\frac{2}{3}V_{dc}+j\frac{\sqrt{3}}{3}V_{dc}$	$-V_{dc}$	0	$-\frac{V_{dc}}{2}$	$-\frac{1}{2}V_{dc}+j\frac{\sqrt{3}}{6}V_{dc}$	$-\frac{V_{dc}}{2}$	$-V_{dc}$	$-\frac{V_{dc}}{2}$	$\frac{1}{6}V_{dc}-j\frac{\sqrt{3}}{6}V_{dc}$
$-\frac{V_{dc}}{2}$	$-\frac{V_{dc}}{2}$	0	$-\frac{1}{6}V_{dc}-j\frac{\sqrt{3}}{6}V_{dc}$	$-\frac{V_{dc}}{2}$	$-\frac{V_{dc}}{2}$	$\frac{V_{dc}}{2}$	$-\frac{1}{3}V_{dc}-j\frac{\sqrt{3}}{3}V_{dc}$	$-\frac{V_{dc}}{2}$	$-\frac{V_{dc}}{2}$	$-\frac{V_{dc}}{2}$	0
$-\frac{V_{dc}}{2}$	$-\frac{V_{dc}}{2}$	V_{dc}	$\frac{1}{6}V_{dc}+j\frac{\sqrt{3}}{6}V_{dc}$	$-\frac{V_{dc}}{2}$	$-\frac{V_{dc}}{2}$	$-V_{dc}$	$-\frac{1}{2}V_{dc}-j\frac{\sqrt{3}}{2}V_{dc}$				

3. OPTIMIZING DUTY RATIO FOR MPCC USING EXPLICIT INTEGRATION APPROXIMATIONS

In a conceptual sense, Model Predictive Current Control represents a novel approach to nonlinear current control in three-phase inverters. This predictive control method effectively manages the output current and voltage of the inverter with high dynamics, circumventing the challenges associated with the nonlinear nature of semiconductor power

converters. The underlying principle of this technique lies in generating a limited number of voltage levels at the output of the cascaded H-bridge inverter [12].

By employing an explicit integration approximation, the forthcoming of the load current prediction is represented in terms of the discrete-time equation, offering a simplified derivative approximation to establish the discrete-time model. The derived approximation is expressed as follows [14]:

$$\dot{x} = \frac{x(k+1)-x(k)}{T_{sp}} \tag{9}$$

Here, T_{sp} denotes the sampling time, k represents the sampling of the present time, and the state variable is x. By substituting current derivative on the grid-side $^{di}/_{dt}$ with explicit integration approximation, the derivative can be approximated as follows:

$$\frac{di}{dt} \approx \frac{i(k+1)-i(k)}{T_{sp}} \tag{10}$$

Now, by substituting (10) into (8), the discrete model of the system is derived as follows:

$$V(k) = L\frac{i(k+1)-i(k)}{T_s} + Ri(k) + e(k) \tag{11}$$

Furthermore, based on (11), the future value of the output current can be obtained by:

$$i(k+1) = \frac{T_s}{L}\big(v(k) - e(k)\big) + i(k)(1 - \frac{RT_s}{L}) \tag{12}$$

3.1. Cost Function

As depicted in *figure 3* and *figure 4*, the controller relies on the cost function requiring predicted output currents $i(k+1)$. This function utilizes any permissible output to bring the controlled currents into closer alignment with their reference values. The future value of the grid side current, $i(k+1)$, is forecasted for all 61 potential switching states generated by the inverter. To achieve this, the prevailing grid side current must be measured. After acquiring the predictions, a cost function (g), as expressed in Equation (13), is evaluated for each switching state. The primary objective of the current control scheme is to minimize the discrepancies between the reference currents and the measured values. This necessity is formulated in the shape of a cost function. Consequently, in the subsequent sampling period, the switching state (and thus the rectangular voltage generated by the FTTCHB inverter) that

minimizes g is chosen and applied. If $g = 0$, the reference current equals its output current. Therefore, the Optimization Cost Function aims to attain a g value as close as possible to zero. Subsequently, the rectangular voltage minimizing the cost function is selected and implemented in the next sampling instance [13], [15].

$$g = f(i_{ref}(k+1), i(k+1)) \tag{13}$$

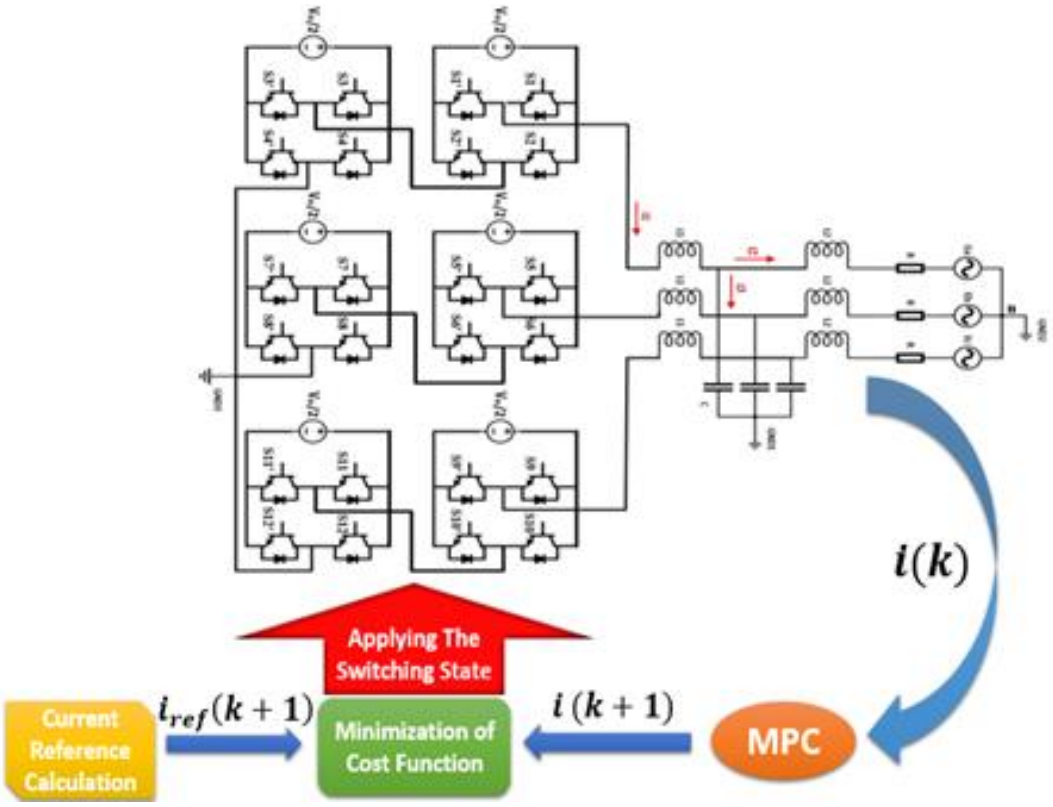

Figure 3. Control strategy of FTT CHB inverter interfaced with an LCL filter and connected to the grid

In the depicted controller shown in *figures 3 and 4*, the cost function (g) necessitates minimizing the predicted currents $i(k+1)$ of the output to minimize errors between measured values and reference currents. The objective of optimizing this cost function is to bring the value of g as close to zero as possible. Consequently, the rectangular voltage is selected and substituted at the instant of the next sampling to reduce the cost function [11], [13]. The subsequent current value is determined by employing Lagrange quadratic extrapolation [16].

$$i_{ref}(k+1) = \Sigma_{l=0}^{n}(-1)^{n-1}\binom{n+1}{l} i_{ref}(k+1-n) \tag{14}$$

For $n \geq 2$ is recommended as sinusoidal reference [10]. Hence, the prediction value with $n = 2$ can be obtained from:

$$i_{ref}(k+1) = 3i_{ref}(k) - 3i_{ref}(k-1) + i_{ref}(k-2) \tag{15}$$

The cost function can be formulated in absolute terms by assessing the error between the reference currents and the predicted currents:

$$g = \left|Re[i_{ref}(k+1) - i(k+1)]\right| + \left|Im[i_{ref}(k+1) - i(k+1)]\right| \tag{16}$$

The cost function, given by equation (16), aims to minimize the error in the output current by utilizing the predicted value $i(k+1)$ from equation (12) and the reference current Iref derived from (15). Consequently, the optimal rectangular voltage can be identified through this process:

$$V_{opt} = V(\min\{g_n\})(n = 0,1,2,\dots,124) \tag{17}$$

where g_n is varietal switching states for the cost function and $V(\min\{g_n\})$ is the optimal cost function of rectangular voltage.

3.2. Optimal Duty Cycle

Within the framework of MPCC, out of 125 rectangular voltages, only 120 non-zero rectangular voltages are required for analysis in equation (16). This is because zero and non-zero rectangular voltages are simultaneously chosen during a single time period. Therefore, accurately calculating the duration of the non-zero rectangular voltage is crucial for system control. The gradients of the grid-side current corresponding to the non-zero voltage vector S_1 and the zero voltage vector S_1 can be readily computed using equation (17) [17], [18].

$$s_1 = \frac{V_{n-z} - e - Ri}{L} \tag{18}$$

$$s_0 = \frac{-e - Ri}{L} \tag{19}$$

The optimal voltage vector, denoted as V_{n-z}, minimizing the cost function, is utilized in the calculation of the output current at the end of the subsequent control cycle.

$$i_{ref}(k+1) = i(k) + \frac{T_{opt}[V_{n-z} - e(k) - Ri(k)] + T_z[V_z - e(k) - Ri(k)]}{L} \tag{20}$$

$$T_{opt} + T_z = T_{sp} \tag{21}$$

$$V_{n-z} + V_z = V(k) \tag{22}$$

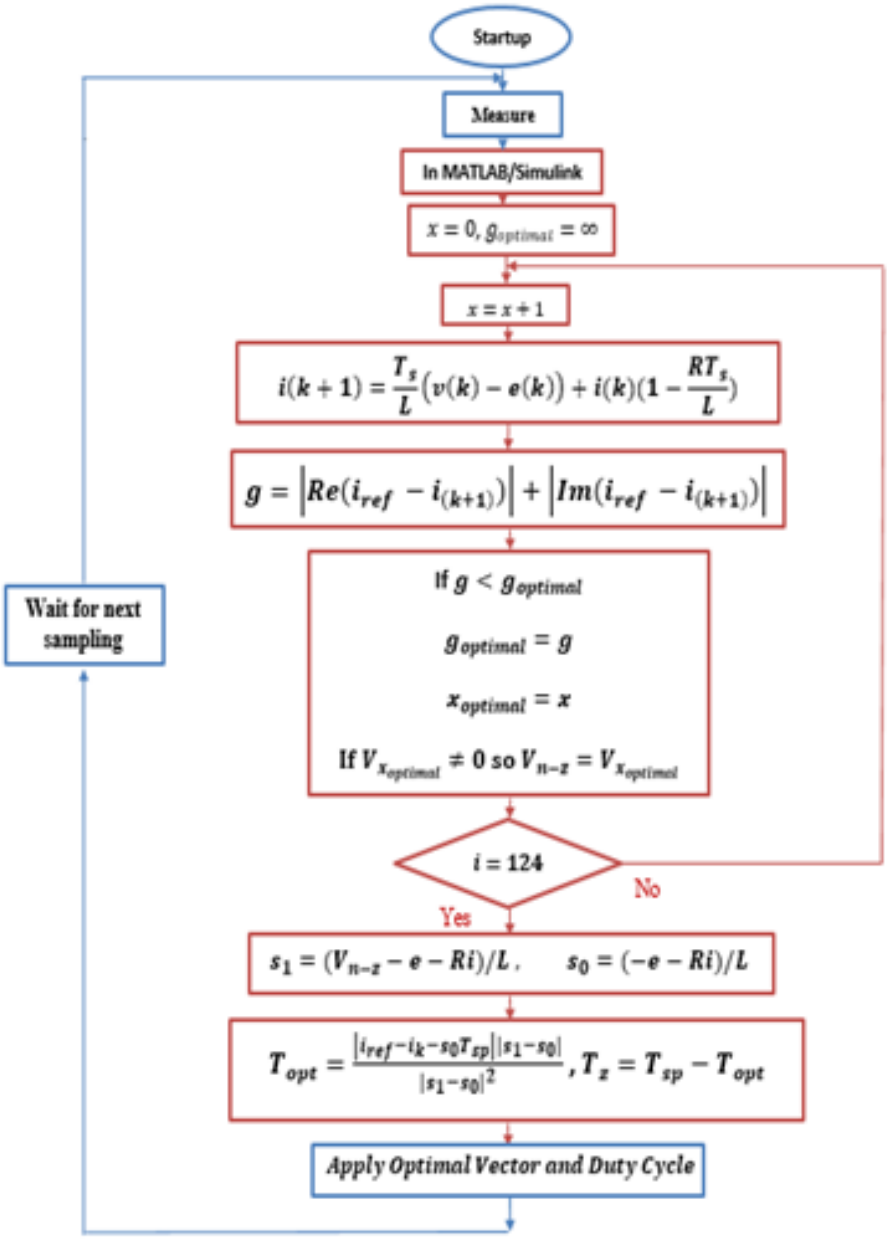

Figure 4. A flow chart illustrating the proposed optimal duty cycle of MPCC

By substituting equations (18) and (19) into equation (20), the output current at the conclusion of the subsequent control cycle can be obtained.

$$(k+1) = i(k) + s_1 \times T_{opt} + s_0 \times (T_{sp} - T_{opt}) \tag{23}$$

The optimal duration, T_{opt}, which minimizes the cost function over a control period, adheres to the following condition.

$$\frac{\partial g}{\partial T_{opt}} = 0 \tag{24}$$

By substituting (23) into (16) and resolving (24), the length of the non-zero rectangular duration can be expressed [19].

$$T_{opt} = \frac{|i_{ref} - i(k) - s_0 \times T_{sp}|}{|s_1 - s_0|} \tag{25}$$

$T_{opt} = 0$, only if $T_{opt} < 0$, and $T_{opt} > T_{sp}$; then, it will be equaled to T_{sp} [20] [21].

3.2. LCL Resonance Damping

The primary circuit of a phase LCL output filter for an inverter is illustrated in *figure 5 (a)*, and its simplified version is presented in *figure 5(b)*, featuring the inductor L_1 on the inverter side, the smoothing capacitor C, and the inductor L_2 on the grid side. In *figure 6 (a)*, a Bode diagram (BD) of the LCL filter without damping is displayed.

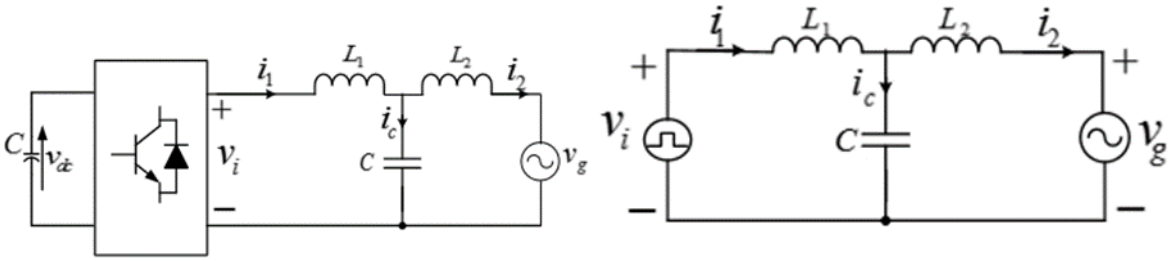

(a) Main circuit *(b) Generic circuit*

Figure 5. A grid-connected system featuring a phase LCL smoother

Considering the transfer function denoted as $H_S = i_2/v_i$, assuming the voltage across the grid system at the point of common coupling (PCC) is an ideal source voltage capable of attenuating all integral multiples of frequencies. When focusing on the inverter-controlled current and assuming V_g is zero, the transfer function can be expressed as follows:

$$i_2 = i_1(s^2 L_2 C + 1)^{-1} \tag{26}$$

$$i_1 = i_2(s^2 L_2 C + 1) \tag{27}$$

$$v_i = i_1\left(sL_1 + \frac{sL_2}{s^2L_2C+1}\right) \tag{28}$$

Substituting equation (2) into (3), we have;

$$0 = {}^{i_2}/_{v_i}\left[(s^2L_2C + 1)\left(sL_1 + \frac{sL_2}{s^2L_2C+1}\right)\right] \tag{29}$$

Therefore, the transfer function

$$H_{(s)} = i(s)v(s)^{-1} = [s^3L_1L_2C + s(L_1{+}L_2)]^{-1} \tag{30}$$

is obtained from equation (4), otherwise;

$$H_{(s)} = [sL_1L_2C(s^2 + \omega_r^2)]^{-1} \tag{31}$$

where $\omega_r = \left(\sqrt{L_1L_2C}\right)^{-1} \cdot \sqrt{L_1{+}L_2}$ and $f_r = {}^{1}/_{2\pi}\,\omega_r$.

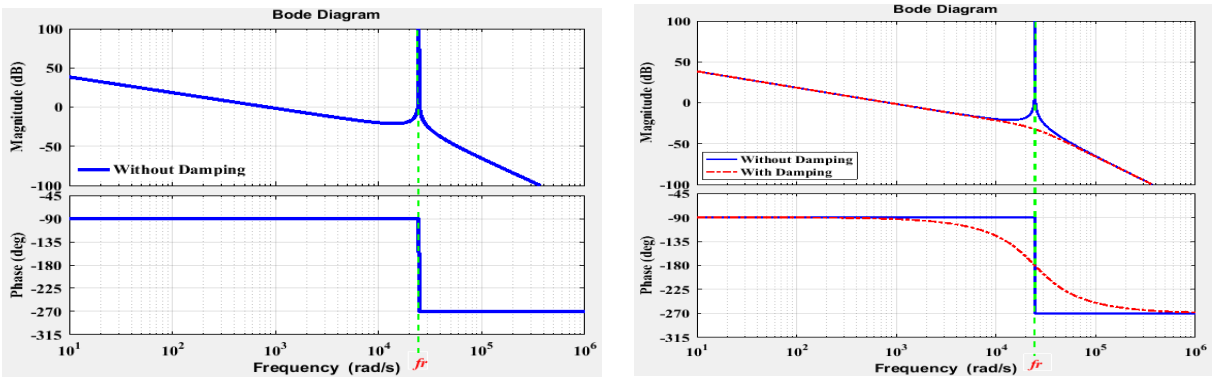

(a) *LCL smoother without damping term* *(b) LCL smoother with damping term*

Figure 6. Bode characteristic representation of LCL smoother

The rapid decrease of -180 at the oscillatory frequency is a result of the LCL smoother oscillation, accompanied by a significant peak magnitude in resonance. This situation poses a potential risk of system instability from a control standpoint [25]. Given that -180 represents a negative crossing, it leads to the formation of complex poles with a pair of closed-loop right-half poles. Introducing damping to subdue the resonance below the $0\ dB$ negative crossing helps avoid these issues. The damping ratio ζ, a first-order term associated with s, is incorporated into the oscillatory term $s^2 + \omega_r^2$ of equation (30) to achieve this.

The dashed lines depicted in *figure 6 (b)* represent the $H_{damp(s)}$ plot. The inclusion of the damping term in the plot demonstrates that while the magnitude and frequency characteristics of the resonance remain unaltered, the oscillatory peak of the smoother is

notably diminished.

3.2.1. LCL Resonance damping: Resistor connected in series with the capacitor

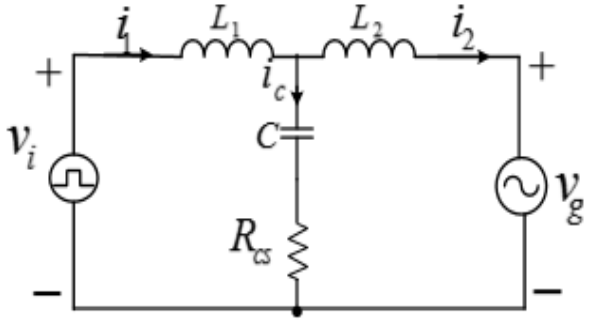

Figure 7. LCL damping technique employing series resistor (R_{cs}) – capacitor (C) connection

The difficulties in controlling the output LCL filter of the Active Power Filter (APF) connected inverter stem from resonance issues. This leads to a sudden -180-degree phase shift with a pronounced resonance peak at the resonance frequency. In [26][27], the paper conduct a thorough examination of various LCL resonance damping methods. Six distinct passive damping strtegies, along with their transfer functions and corresponding Bode diagrams, are scrutinized and contrasted for analysis. The resistor placed in series with capacitor as shown in the figure below is recommended in practice and its corresponding transfer function is given as:

$$H_{R_{cs}(s)} = i(s)v(s)^{-1} = (sR_{cs}C + 1)[s^3(L_1L_2C + s^2R_{cs}(L_1{+}L_2) + s(L_1{+}L_2)^{-1}] \quad (32)$$

4. SIMULATION RESULTS

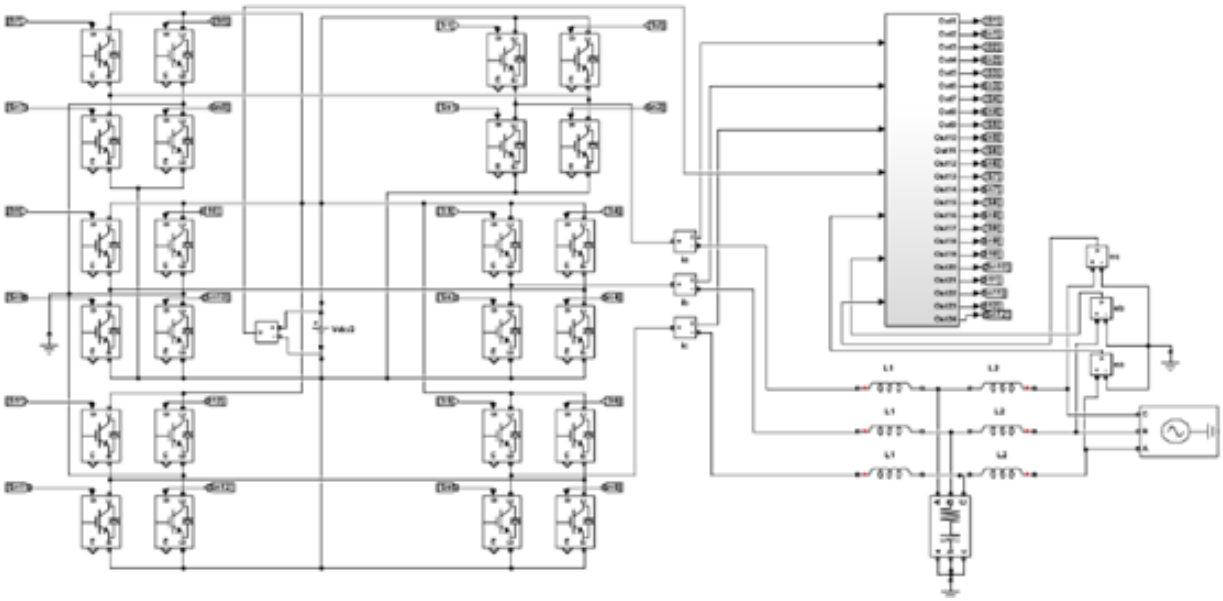

Figure 8. MPCC control strategy for FTT CBH gird-interactive inverter with LCL smoother output

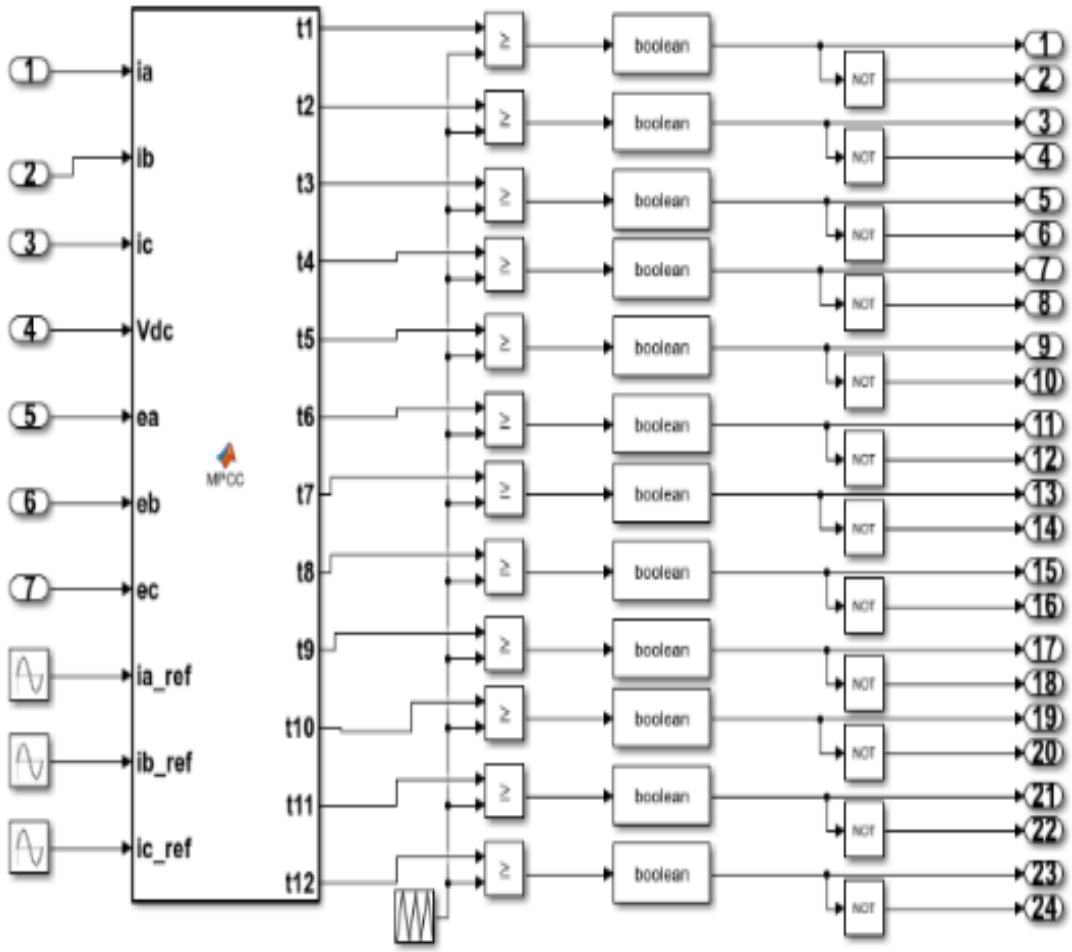

Figure 9. MPCC subsystem with modification

Table 2. Parameters employed for both the simulation and laboratory set-up [21]

Specification for MATLAB Simulation and Laboratory Setup				
Parameters used for the simulation			***Material/specifications for laboratory setup***	
Variable	***Parameters of the system***	***Value***	***Materials***	***Description/Specifications***
V_{dc}	DC-Link voltage	700V	DC Source	Variable 1000 V DC
e	Grid Voltage (RMS)	220V	Gate Drivers	IGBT GD C044BG400 series
f	Line voltage frequency	50Hz	DSP & GUI	32-bit TMS320F28335, 20 kHz
i_{ref}	Reference current peak amplitude	20A	GRID	Variable 700 V AC
L_2	Filter inductance	1mH	LCL filter	400 V AC, 2.5 kHz SF
L_1	Filter Inductance	3mH	Five level three-phase cascaded full bridge inverter	Laboratory built
C_f	Filter Capacitance	15μF	Oscilloscope	Tektonix Mixed Domain
R_f	Filter Resistance	10Ω	Materials	Description/Specifications
T_{sp}	Sampling time	25 to 100 μs		

Simulation models and diverse experiments are employed to validate the performance attributes of the suggested duty ratio optimization for MPCC control techniques applicable to

a five-level three-leg three three-phase (FTT) CHB grid-interactive inverter with LCL smother output, as outlined in Table 2. To facilitate comparison, the outcomes of the conventional MPCC will also be utilized. *Figure 10* illustrates the proposed MPCC with duty cycle optimization.

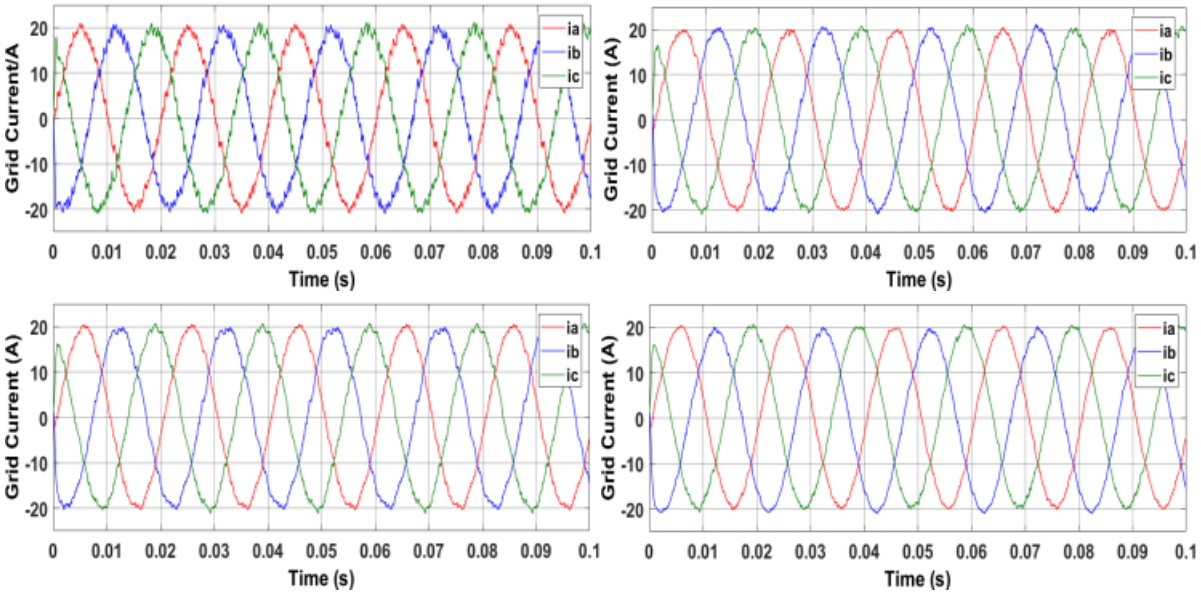

(a) *(b)*

Figure 10. Waveforms from simulation of FTT CHB using explicit integration approximation. (a) The conventional MPCC at the sampling time of 50μs and 25μs, (b) The proposed MPCC with optimal duty cycle at the sampling time of 50μs and 25μs.

Upon comparing the conventional and proposed approaches, as depicted in *figure 10* with regards to grid current waveforms, it is evident that the conventional method exhibits more pronounced distortion in the output current compared to the proposed method. Consequently, the novel method demonstrates reduced current harmonics and lower current ripple.

Another noteworthy observation is apparent in *figure 11*. The Total Harmonic Distortion (THD) for the proposed MPCC is 1.65% and 1.1%, representing a substantial improvement over the 3.11% and 1.42% recorded for conventional MPCC at sampling times of $T_{sp} = 50\mu s$ and $T_{sp} = 25\mu s$, respectively. Once again, the proposed method proves to be effective and efficient, producing output waveforms that closely resemble sinewaves.

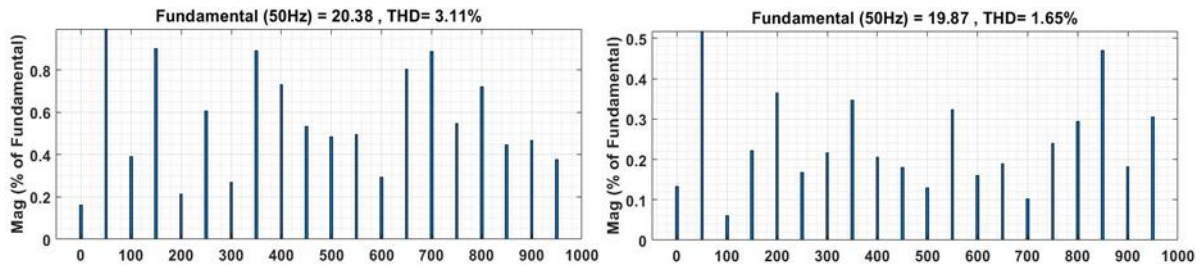

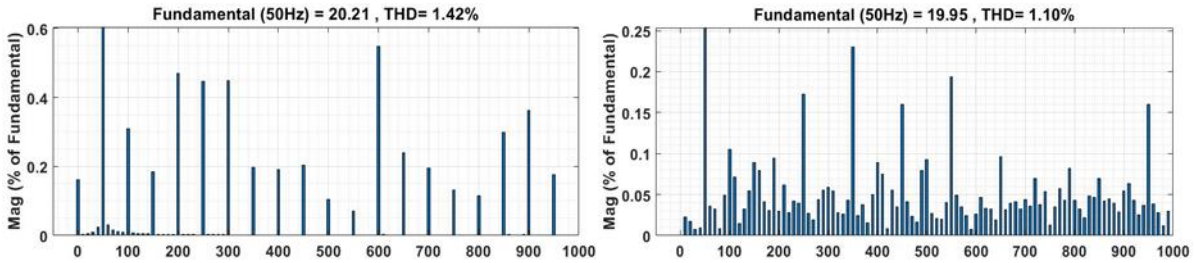

(a) *(b)*

Figure 11. Harmonic spectrum examination of a FTT CHB utilizing explicit integration approximation. (a) MPCC of traditional characteristics at the sampling time of 50µs and 25µs, (b) MPCC with enhanced duty cycle at the sampling time of 50µs and 25µs

Figure 12 illustrates the stability of the proposed method, showcasing a more precise tailing of the output current to its reference. Even in the face of altering the output current, the proposed method exhibits superior accuracy and fewer ripples compared to the traditional method.

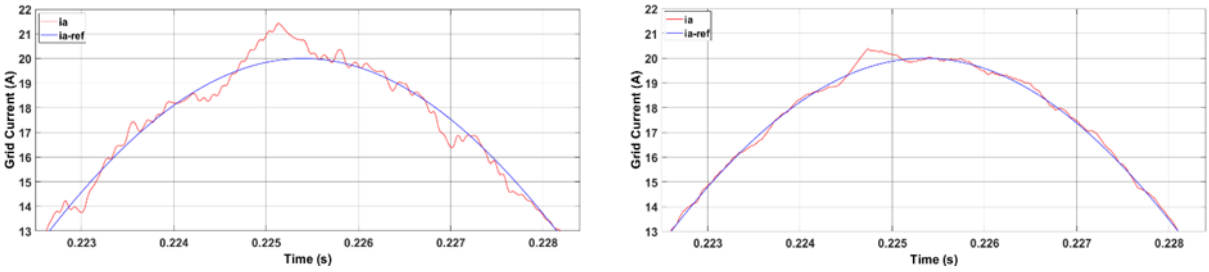

Figure 12. Grid current representation at the 50µs sampling time employing an explicit integration algorithm. (a) The traditional MPCC, (b) Duty cycle control of the modified MPCC

A bar graph depicting the grid current total harmonic distortion (THD) with varying sampling times for both conventional and proposed methods is presented in *figure 13*. It is evident that the proposed method exhibits considerably lower THD values compared to the conventional method, attributed to the duty cycle optimization employed in the proposed Model Predictive Current Control (MPCC). Consequently, the proposed MPCC demonstrates substantial advantages, particularly in applications with increased sampling time.

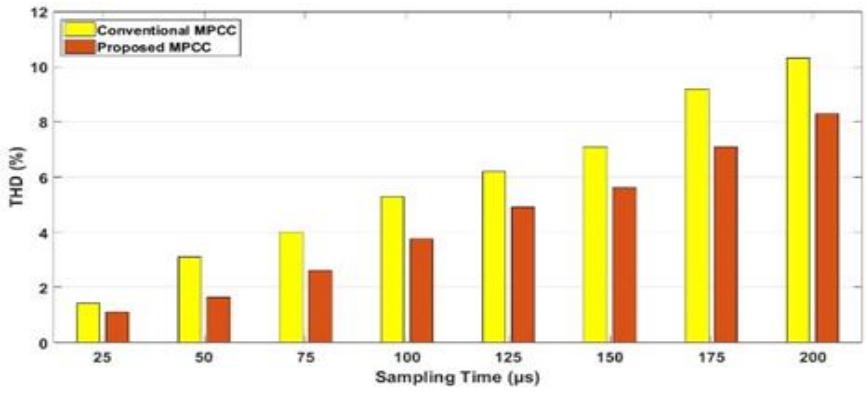

Figure 13. Comparative simulation outcomes of THD in Grid Current for the conventional and proposed MPCC.

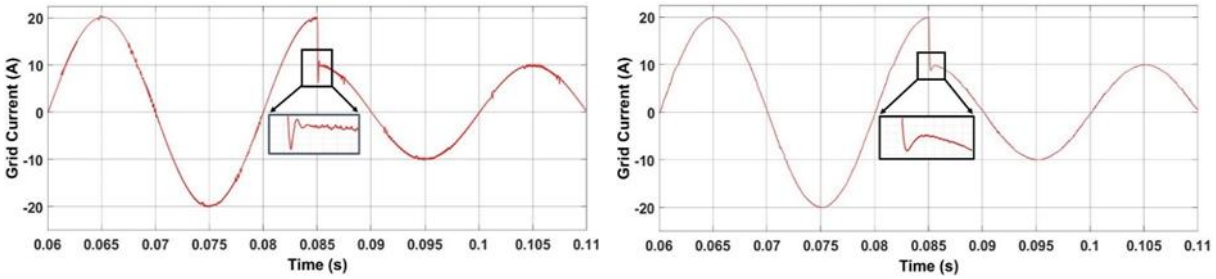

(a) *(b)*

Figure 14. Disruption of the reference current, transition from 20 A to 10 A in phase A of grid current. (a) The traditional MPCC. (b) Modified MPCC with duty cycle control

Results pertaining to reference current step changes indicate that the output current, without a step change, swiftly reaches its reference (see f*igure 14*). In contrast, the conventional method displays a weaker connection with the dynamic response when subjected to step alterations.

The Bode characteristic transfer function is shown *figure 15* where we can observe that the harmonic attenuation ability is better in many frequency ranges as a result of adding a resistor in series with the capacitor of LCL filter.

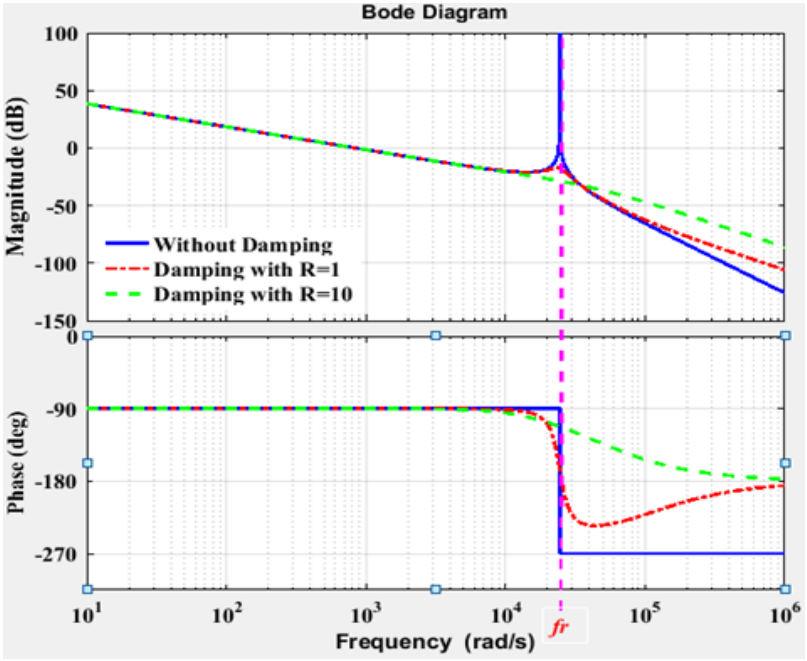

Figure 15. Bode characteristic representation of series resistor-capacitor damping technique

5. EXPERIMENTAL SETUP

To validate the simulation model's realization, an experimental setup featuring a three-level three-leg three-phase CHB grid-interactive inverter with LCL filter output is

implemented in the laboratory, as depicted in *figure 16* and material/specifications captured in Table 2. The experimental prototype system is configured with the algorithm of the proposed MPCC. A 20 kHz TMS320F28335 digital signal processor with 32-bit floating characteristics serves as the platform for the control system, where the coded proposed MPCC algorithm is executed. The parameters, consistent with simulation parameters, are summarized above, and a Tektronix Mixed Domain Oscilloscope (MDO3014) is employed as the measuring equipment.

The experimental and experimental results exhibit some similarities; however, as depicted in *figure 17*, the silhouette of the output current waveforms from the simulation is notably superior and clearer compared to the experimental counterpart. This discrepancy is attributed to the sinusoidal and constant grid voltage employed in the simulation. Nevertheless, it's noteworthy that the output current waveform of the proposed method is smoother than that of the conventional method. *Figure 18* illustrates the Total Harmonic Distortion spectrum for the proposed and convention techniques, indicating values of 4.47% and 2.72%, respectively. Thus, the proposed techniques outperforms the traditional strategy significantly. In summary, the effecacy of the proposed technique has been validated through both simulation as well as experimental results.

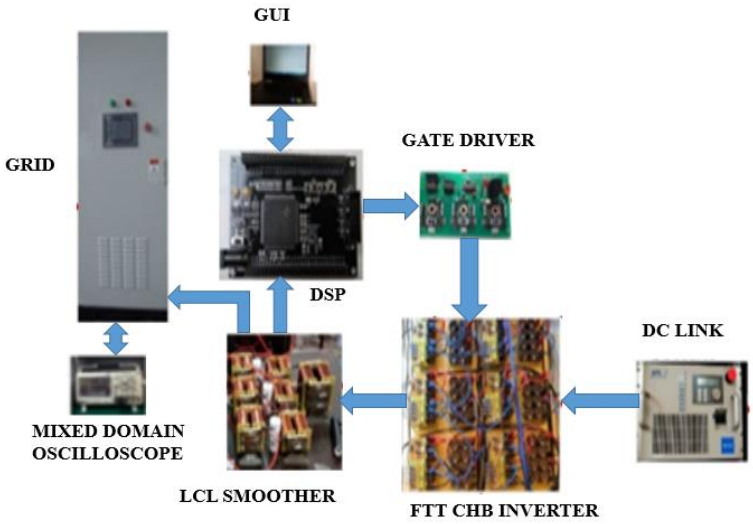

Figure 16. Experimental set-up

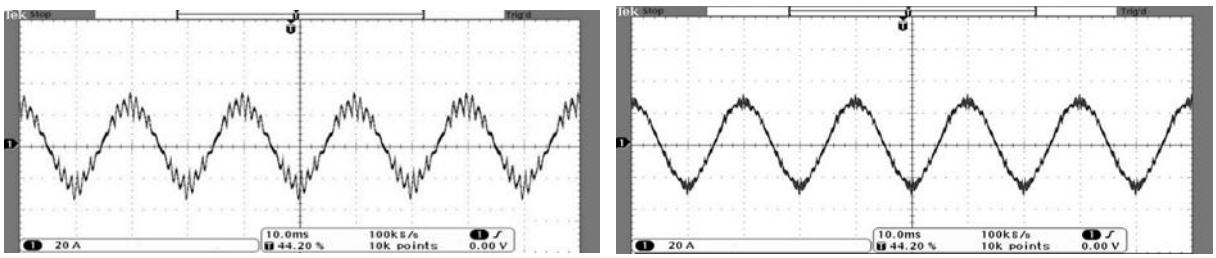

(a) Coventional MPCC *(b) Proposed MPCC*

Figure 17. Waveforms of the three-phase output current

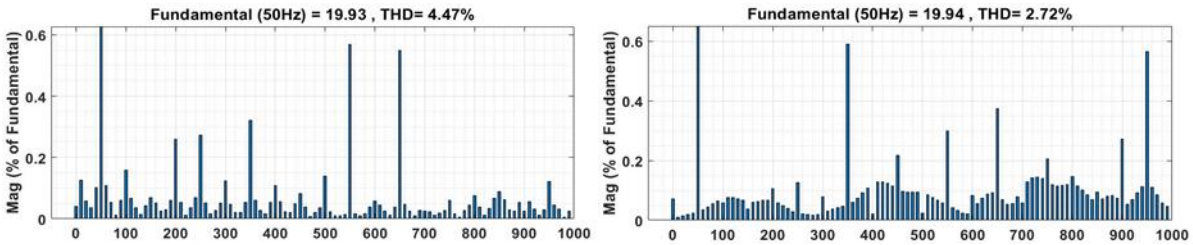

(b) Coventional MPCC *(b) Proposed MPCC*

Figure 18. THD spectrum of the grid current

6. CONCLUSION

In this study, we delved into the intricacies of a five-level three-leg three-phase cascaded H-Bridge (FTTCHB) inverter and devised a Model Predictive Current Control (MPCC) technique tailored for this specific inverter configuration when interfaced with the grid through an output LCL smoother. The evaluation of MPCC for a FTTCHB inverter connected to the grid involved a thorough examination across different sampling times. Our approach systematically scrutinized each of the 61 potential switching states, aiming to identify the state that minimizes the cost function and consequently opting for the one with optimal switching characteristics. To optimize steady-state performance, the proposed MPCC technique necessitates the simultaneous application of both zero and nonzero vectors within a single control period. Ultimately, we conducted simulation and experimental assessments to affirm the efficacy of the proposed MPCC, employing optimal duty cycles and leveraging the explicit integration approximation.

REFERENCES

[1] B. N. L. Ande, N. R. Tummuru, R. T. Pogulaguntla, and B. Ravada, "A Grid-Interactive Power Conversion System for Integrating the PV-Wind Energy Sources," *IEEE Syst. J.*, vol. 16, no. 2, pp. 1851–1860, 2022, doi: 10.1109/JSYST.2021.3071291

[2] A. Raef, A. S. Al-Sumaiti, A. Ibrahim, I. V. Alexandrov, A. G. Garganeev, and A. A. Z. Diab, *Assessment of Model Predictive Voltage Control for Autonomous Four-Leg Inverter*, *IEEE Access*, vol. 8, pp. 101163–101180, 2020, doi: 10.1109/ACCESS.2020.2996753.

[3] A. Goudarzian and A. Khosravi, *Voltage Regulation of a Negative Output Luo Converter Using a PD-PI Type Sliding Mode Current Controller*, International Journal of Engineering, Transaction B: Applications, Vol. 32, No. 2, (2019), 277-285.

[4] X. L. B. Dong, *Improved Variable Switching Frequency Control for Capacitor Voltage Ripple Regulation in Multilevel Flying Capacitor Converter, IEEE Trans. Power Electron*, vol. 38, no. 5, pp. 5700–5705, 2023.

[5] Franquelo, L. G., Rodríguez, Leon, J., Kouro, J. I. S., Portillo, R. & Prats, M. A. M., *The age of multilevel converters arrives*, IEEE Industrial Electronics Magazine, vol. 2 No. 2, (2008) 28–39.

[6] G. Sridhar, P. SatishKumar and M. Sushama, *A Novel Generalized Topology for Multi-level Inverter with Switched Series-parallel DC Sources (RESEARCH NOTE)*, International Journal of Engineering, Transaction C: Aspects, Vol. 30, No. 6, (2017), 851-858.

[7] Alireza Nami and Firuz Zare. *Multilevel Converters in Renewable Energy Systems*, Renewable Energy, T J Hammons (Ed.), (2009).

[8] J. Wen and K. M. Smedley, *Synthesis of Multilevel Converters Based on Single- and/or Three-Phase Converter Building Blocks,* IEEE Trans. Power Electron., vol. 23, no. 3, (2008) 1247–1256.

[9] Patricio Cortés, Gabriel Ortiz, Juan I. Yuz, José Rodríguez, Sergio Vazquez and Leopoldo G. Franquelo, *Model Predictive Control of an Inverter With Output LC Filter for UPS Applications*, IEEE TRANSACTIONS ON INDUSTRIAL ELECTRONICS, vol. 56, (2009), 1875-1883.

[10] Jose Rodriguez, Patricio Cortes, *Predictive control of power converters and electrical drives*, Wiley-IEEE Press (2012).

[11] Sung-Yeul Park, Jih-Sheng Lai, Woo-Cheol Lee, *An Easy, Simple, and Flexible Control Scheme for a Three-Phase Grid-Tie Inverter System*, Energy Conversion Congress and Exposition (ECCE), IEEE Press, (2010), 599-603.

[12] PASTOR Marek, DUDRIK Jaroslav, *Grid-tied Multilevel Inverter With Predictive Current Control*, Journal of Electrical and Electronics Engineering, Volume 5, Number 1, (2012), 173-178.

[13] J. Rodriguez, B. Wu, M. Rivera, C. Rojas, V. Yaramasu , A. Wilson, *Predictive Current Control of Three-Phase Two-Level Four-Leg Inverter*, 14th International Power Electronics and Motion Control Conference (EPE-PEMC), IEEE Press, (2010), 106-110.

[14] Yongchang Zhang, Changqi Qu, Zhengxi Li, Yingchao Zhang, Longhan Cao, *Direct Power Control of PWM Rectifier With Optimal Duty Ratio Under Unbalanced Network*, Power Electronics and ECCE Asia (ICPE-ECCE Asia), IEEE Press, Jun. (2015), 1116 – 1122.

[15] Almaktoof A. M., Raji A. K., & Kahn M. T., *Finite-Set Model Predictive Control and DC-Link Capacitor Voltages Balancing for Three-Level NPC Inverters*, Proceeding of the 16th International Power Electronics and Motion Control Conference and Exposition (PEMC 2014), IEEE Press, (2014), 224 – 229.

[16] Marek Pástor, Jaroslav Dudrik, *Predictive Current Control of Grid-tied Cascade H-bridge Inverter*, ATKAFF, Vol. 54, No. 3, (2013), 308–315.

[17] [Y. Zhang, W. Xie, Z. Li and Y. Zhang, *Model predictive direct power control of a PWM rectifier with duty cycle optimization*, IEEE Trans. Power Electron., vol. 28, no. 11, (2013), 5343-5351.

[18] Yongchang Zhang and Yubin Peng, *Model Predictive Current Control with Optimal Duty Cycle for Three-Phase Grid-Connected AC/DC Converters*, Power Electronics and Application Conference and Exposition (PEAC), IEEE Press, (2014), 837 – 842.

[19] V. Yaramasu, M. Rivera, M. Narimani, B. Wu and J. Rodriguez, *High performance operation for a four-leg NPC inverter with two-sample-ahead predictive control strategy*, Electric Power Systems Research, vol. 123, (2015), pp. 31–39.

[20] Yongchang Zhang, Yubin Peng and Bo Xia, *Efficient model predictive control with optimal duty*

cycle for power converters, Power Electronics and Motion Control Conference (IPEMCECCE Asia), IEEE Press, (2016), 1076 - 1083.

[21] E. K. Adjei-Saforo, E. A. Frimpong, F. B. Effah, M. Adam, E. Shahrous, and S. Hongsheng, *Duty Ratio Optimization for a Multi-Level Poly-phase Cascaded H-Bridge Grid-Interactive Inverter Using Model Predictive Current Control Based on Explicit Integration Algorithm, 2023 IEEE AFRICON Conference*, Nairobi, Kenya, 2023. [CrossRef]

[22] S. Mariethoz and M. Morari, *Explicit model-predictive control of a pwm inverter with an lcl filter*, IEEE Trans. Ind. Electron, vol.56, (2009), 389-399.

[23] O. Rivera, M. Mauledoux, A. Valencia, R. Jimenez and O. Avilés, *Hardware in Loop of a Generalized Predictive Controller for a Micro Grid DC System of Renewable Energy Sources*, International Journal of Engineering, Transaction B: Applications, Vol. 31, No. 8, (2018), 1215-1221.

[24] M. Arehpanahi and D. Paknia, "A New Single-phase Symmetrical Cascade Multilevel Inverter with Low Number of Power Switches", *Hardware in Loop of a Generalized Predictive Controller for a Micro Grid DC System of Renewable Energy Sources*, International Journal of Engineering, Transaction B: Applications, Vol. 31, No. 8, (2018), 1228-1233.

[25] H. A. Salama, S. J. Finney, and B. W. Williams, *Predictive Control of LCL Filters for Grid-Connected Inverters*, IEEE Transactions on Industrial Electronics, Vol. 68, No. 3, pp. 2192-2202, Mar. 2021.

[26] E. K. Adjei-Saforo, M. Adam, S. A. Darko, S. N. Akansake, *Comparative Studies into Resonance Damping of Output LCL Filter For Active Power Filter With Voltage Source Inverter*, International conference on Applied Sciences and Technology (ICAST),pp. 98-109, 2024. [CrossRef]

[27] M. Adam, S. Ebrahimpanah, Y. Chen and Q. Chen, "Performance of CLC Filters with Shunt APF for Harmonic Current Mitigation", DEStech Transaction on Engineering and Technology research, Vol. 2017/15935, pp.32-41, 2017